TECHNISCHE UNIVERSITÄT MÜNCHEN

WALTHER - MEISSNER - INSTITUT FÜR TIEF - TEMPERATURFORSCHUNG

BAYERISCHE AKADEMIE DER WISSENSCHAFTEN

3D Cavities for Circuit Quantum Electrodynamics

Bachelor's Thesis

Jonathan Rupert Ayang Müller

Supervisor: Prof. Dr. Rudolf Gross

Munich, July 2014

Contents

Chapter 1

Introduction

Quantum information science is nowadays considered to be one of the most revolutionary fields of research in modern physics and computer science, promising to be able to solve a whole category of computational problems quicker than any classical computer ever could [1]. The key to construct such a device will be to implement and control quantum bits (qubits, quantum mechanical two-level systems) in a scalable way. Several approaches have been taken in creating different realizations of qubits, such as Rydberg atoms, electron spins, photons or Josephson-junction based superconducting circuits [2]. In particular the latter platform allows one to investigate the light-matter interaction by placing such a qubit circuit inside a microwave resonator, where it acts as an artificial two-level atom. This setup is called circuit quantum electrodynamics (QED) [3–5] and features large coupling strengths [6] as well as a high degree of control.

The main restriction in circuit QED are the qubit coherence times, which describe how long a qubit is able to maintain its given state. Several causes ("decay channels"), which shall not be further explored at this point, contribute to qubit decoherence. However, one of them is the participation ratio of the electric field at the lossy metal-substrate interface of the qubit wafer.

Previously, qubit lifetimes in traditional planar resonators were restricted to up to $44\,\mu\mathrm{s}$ [7], heavily compromising their usefulness. A recent innovation has been the use of three-dimensional (3D) instead of the traditionally planar resonators, which severely reduce the aforementioned participation ratio due to the increased mode volume of the electric field and push for qubit lifetimes times exceeding $0.1\,\mathrm{ms}$ [8–10].

Another key property of 3D resonators are the decreased internal losses [11–13]. The goal of this thesis is to characterize a 3D cavity with regard to its use in circuit QED. In particular, this implies a study of the temperature dependence of the internal Q factor and the tunability of the external Q factor.

In the next chapter, the theoretical foundations for the use of 3D cavities are established. First, we introduce the rectangular geometry of the resonator and the resulting electromagnetic eigenmodes. The formula for their resonance frequencies is given, and the need as well as possible approaches for frequency tuning are discussed.

Afterwards, important quantities such as S-parameter and Q factor are defined.

In Ch. 3, we introduce the two cavity prototypes manufactured for this thesis, highlighting multiple important properties by providing the necessary background as well as motivating experiments in order to characterize them further. Next, two setups for frequency tuning are presented. Furthermore, details regarding the technical setup for microwave generation and measurement, as well as cooldown methods are given.

In Ch. 4 we present and discuss the results of the previously described experiments, and the efficiency of the frequency tuning methods is verified. Special emphasis is put on the data gathered during the cooldown of the cavity to millikelvin temperatures, where the quality factor of the first of the two prototype cavities is determined to $Q_\mathrm{L} = 3.4 \cdot 10^5$.

The final chapter summarizes the insights gained from this thesis, and focuses on improvements to be done in the near future, also proposing two simple methods that enable in-situ frequency tuning at millikelvin temperatures.

Chapter 2

Theory

First of all, we briefly cover the theoretical background necessary for measurement and analysis of the 3D resonator. Furthermore, the desired properties of the resonator such as high quality factors and frequency tunability are discussed.

2.1 3D resonator theory

As outlined in Ch. 1, 3D resonators are shown to enable Q factors exceeding those of traditional planar resonators by orders of magnitude, recently up to $Q_\mathrm{i} = 6.9 \cdot 10^6$. Considering that the larger mode volume and the low surface participation ratio [12, 14, 15] are some of the main advantages of the 3D resonator, it seems natural to use a very simple geometry, thus minimizing the surface to volume ratio. While there has been research on cylindrical cavities [14], we focus on the much more commonly used rectangular cavity [8–10, 13].

2.1.1 Transverse electric and magnetic eigenmodes

The microwave signal coupled into the resonator generates transverse electric ($\mathrm{TE}_{n_x/n_y/n_z}$) and transverse magnetic ($\mathrm{TM}_{n_x/n_y/n_z}$) eigenmodes, whose resonance frequencies $f_{n_x/n_y/n_z}$ can be easily determined and consequently adjusted via [12, 16]

$$f_{n_x/n_y/n_z} = \frac{c}{2\pi} \sqrt{\left(\frac{n_x \pi}{b}\right)^2 + \left(\frac{n_y \pi}{h}\right)^2 + \left(\frac{n_z \pi}{a}\right)^2}\,, \tag{2.1}$$

with width b, height h and length a, corresponding to the x-, y- and z-dimensions, as well as the propagation speed c inside the cavity. Conventionally, the two antennas for microwave generation and measurement are placed along the z-axis of the cavity.

As their names suggest, the transverse electric and transverse magnetic modes, respectively, indicate that the associated field is perpendicular to the propagation direction. The indices n_x, n_y and n_z specify the number of half-wavelengths in each direction of the field.

The TE mode with the lowest frequency is the TE_{101} fundamental mode, which has a single maximum of the electric field in the very center of the cavity, where eventually the qubit is to be placed. The next higher modes whose electric field at the center qubit position has a finite value and therefore interacts with the qubit are the TE_{301} and TE_{103} modes [9].

The maxima of the TE_{102} mode at $\frac{1}{4}$ and $\frac{3}{4}$ of the length of the cavity are also possible candidates for qubit positions. This positioning would allow for easy daisy chaining of multiple two-qubit cavities, with the qubit in the second maximum of a cavity coupling to the next cavity's first-maximum-qubit and so on.

2.1.2 Frequency tuning

For qubit measurements, the cavity has to feature a very specific resonance frequency f_0 of the mode with an antinode at the qubit position. The desired resonance frequency depends on the transition frequency of the qubit [17, 18]. Moreover, if multiple cavities are to be coupled, it is sometimes desireable that they have the exact same resonance frequency ("frequency degeneracy"). Since imprecisions caused by the manufacturing process of the cavity casing lead to deviating resonance behavior, a method for frequency tuning must be found. The frequency range where the cavity has to be tunable typically spans a few tens of MHz. Another requirement for the cavity tuning mechanism is to cause as little disturbance as possible with characteristics other than the resonance frequency, as to not disturb the measurement.

Equation (2.1) offers two ways for frequency adjustment: either by changing the physical dimensions a, b, h of the cavity or by affecting the propagation speed c, i.e., via dielectric material inside the cavity. By assuming equal length a and width b we can simplify Eq. (2.1) for the TE_{101} mode to

$$f_{101} = \frac{c}{\sqrt{2}a} \, . \tag{2.2}$$

Our cavity has its resonance frequency at $f_{101} = 5.7\,\mathrm{GHz}$, so a reduction by e.g., 20 MHz would pose a decrease in frequency by 0.4 %. With length and width $a = b \approx 3.8\,\mathrm{cm}$ of the cavity, an increase by less than 0.2 mm each would already accomplish the required frequency tuning. Hence, the resonance frequency of the cavity is highly dependent on its physical dimensions.

The same is true for a dielectric material inside the cavity: Using $c = (\epsilon_0 \epsilon_\mathrm{r} \mu_0 \mu_\mathrm{r})^{-1}$, with the vacuum permittivity ϵ_0, the relative permittivity ϵ_r, the vacuum permeability μ_0 and the relative permeability μ_r, it becomes obvious that even materials with a relatively small relative permittivity heavily affect the resonance frequency. Thus, if one is to tune the frequency by inserting a dielectric material, very small amounts of that dielectric will suffice.

2.2 Scattering parameters

In order to determine the resonance frequencies as well as quality factors of the cavity modes, we make use of scattering parameters (S-parameters): the elements of the scattering matrix, which in turn provides a simple way of assessing linear electrical networks — including the 3D resonator fundamental to this thesis.

In multiple-port, linear electrical network, the scattering matrix **S** links the (complex) incident power waves a_i and reflected power waves b_i at port i via [16]

$$\begin{pmatrix} b_1 \\ \vdots \\ b_n \end{pmatrix} = \begin{pmatrix} S_{11} & \dots & S_{1n} \\ \vdots & \ddots & \vdots \\ S_{n1} & \dots & S_{nn} \end{pmatrix} \begin{pmatrix} a_1 \\ \vdots \\ a_n \end{pmatrix} , \tag{2.3}$$

consisting of the complex S-parameters S_{ij} [16]. The ratio of the incident power at port j and outgoing power at port i comes to

$$\frac{P_i}{P_j} = |S_{ij}|^2 . \tag{2.4}$$

2.2.1 Transmission of an ideal two-port resonator

For the two-port resonator we assign the port number $j = 1$ to the input port and $i = 2$ to the output port.

The scattering matrix of a two-port microwave resonator reduces to two dimensions, and the magnitude of the S_{21}-parameter with respect to the frequency of the microwave takes the form of the square root of the Lorentzian function around the resonance peaks [12, 19]

$$\left. |S_{21}(f)|^2 \right|_{f \approx f_0} = \left(\frac{\kappa}{1+\kappa} \right)^2 \frac{\gamma^2}{(f - f_0)^2 + \gamma^2} , \tag{2.5}$$

with the frequency f, resonance frequency f_0 and full width at half maximum (FWHM) $\Delta f = 2\gamma$. κ is the coupling coefficient introduced in Sec. 2.3.1. The magnitude of $|S_{21}|$ is also called the transmission magnitude.

2.3 Quality factor and photon lifetimes

The quality factor of a resonator is defined by the ratio of energy stored to energy dissipated inside the resonator:

$$Q = 2\pi \cdot \frac{\text{energy stored}}{\text{energy dissipated per cycle}} . \tag{2.6}$$

Thus, the Q factor gives insight to the energy losses of a resonator — a higher Q factor implies lower losses.

In the low damping limit we can determine the Q factor via the inverse of the fractional bandwidth $\frac{\Delta f}{f_0}$ as [16]

$$Q = \frac{f_0}{\Delta f} \tag{2.7}$$

and, hence, calculate Q via the Lorentzian given by Eq. (2.5).

Now we have to distinguish: The internal quality factor Q_i only refers to the power dissipated in the resonator itself, whereas the external quality factor refers to the power dissipated by the external circuit without the resonator. The two can be combined by means of

$$\frac{1}{Q_\mathrm{L}} = \frac{1}{Q_\mathrm{i}} + \frac{1}{Q_\mathrm{c}} \tag{2.8}$$

to obtain the loaded (or total) quality factor Q_L. So by measuring the magnitude of the S_{21}-parameter of a resonator and using Eq. (2.5) and Eq. (2.7) we only receive the loaded quality factor Q_L.

For a rectangular cavity with vacuum inside, the internal quality factor Q_i of the TE_{10n_z} mode can be calculated as [14, 16]

$$\begin{aligned} Q_\mathrm{i} &= \frac{4\pi\eta f_{10n_z}^3}{R_\mathrm{S}\, c^3} \frac{a^3 b^3 h}{2a^3 h + 2{n_z}^2 b^3 h + {n_z}^2 a b^3 + a^3 b} \\ &\propto \frac{f_{10n_z}^3}{R_\mathrm{S}}\,, \end{aligned} \tag{2.9}$$

with according resonance frequency f_{10n_z} and surface resistivity R_S, which is further discussed in Sec. 3.1.1 and Sec. 3.1.2. η is the vacuum impedance. The proportionality factor solely depends on the dimensions of the rectangular cavity and n_z. Note that because of the dependence of the proportionality factor on n_z, as well as the dependence of R_S on f_{10n_z}, higher frequency modes do not inherently produce higher Q factors.

2.3.1 Coupling coefficient

The ratio of internal and external Q factor

$$\kappa = \frac{Q_\mathrm{i}}{Q_\mathrm{c}} \tag{2.10}$$

defines the coupling coefficient κ. So in order to be able to determine the internal quality factor Q_i from the total quality factor Q_L, one has to minimize the coupling coefficient ("under-coupling"), such that:

$$Q_\mathrm{L} \xrightarrow[\kappa \ll 1]{} Q_\mathrm{i} \ . \tag{2.11}$$

Alternatively, the coupling of a symmetrical cavity can be calculated via the S-parameters at resonance frequency using [20]

$$\kappa = \frac{2\,|S_{21}(f_0)|^2}{1 - |S_{11}(f_0)|^2 - |S_{21}(f_0)|^2} \ . \tag{2.12}$$

2.3.2 Photon lifetime

Finally, we can relate the loaded quality factor Q_L to the lifetime τ of the photons inside the cavity via the resonance frequency f_0 by using [14, 21]

$$Q_\mathrm{L} = 2\pi f_0\, \tau \ . \tag{2.13}$$

Ergo, the highest quality factors and thus photon lifetimes are achieved by minimizing the FWHM of the resonance peak of the squared magnitude of the S_{21}-parameter (cf. Eq. (2.7)).

The energy of one photon at resonance frequency is $\boldsymbol{h} f_0$, with the Planck constant $\boldsymbol{h}$. The average number of photons $\bar{n}$ inside the cavity for a given input power P_1 can be estimated by [6]

$$P_1 = \bar{n}\boldsymbol{h}\,\frac{f_0}{\tau} = 2\pi\,\bar{n}\boldsymbol{h}\,\frac{{f_0}^2}{Q_\mathrm{L}} = 2\pi\,\bar{n}\boldsymbol{h}\,f_0 \Delta f \ . \tag{2.14}$$

Another aspect revealed by this equation is the — for a constant photon number $\bar{n}$ — inverse proportionality between required input power P_1 and the loaded quality factor Q_L. For qubit readout, typically only a single photon is desired in the cavity at a time in order to rule out two-photon-processes. So ideally $\bar{n} \approx 1$. However, this means that exceedingly high loaded Q factors require very low input powers, and, hence, very low output powers, which are susceptible to noise. Therefore, resonators for circuit QED are typically constructed to have high internal Q factors and high coupling coefficients, leading to smaller loaded Q factors.

Chapter 3

Experimental methods

In this chapter, we examine the different properties of the two cavities manufactured for this thesis and motivate corresponding experiments. Additionally, details concerning the technical measurement setup are provided.

3.1 Cavity geometry and fabrication

A technical drawing of the cavity casing including dimensions can be found in Fig. A.1 in the appendix. Pictures of the cavity are shown in Fig. 3.1a and Fig. 3.1b. Simulations have shown the Q factor to be optimal for equal length and width, such that $a = b > h$. However, due to the manufacturing process via milling, the cavity is not exactly rectangular — it features two opposing curved sides, also visible in Fig. 3.1b. The cavities studied in this work have length $a = 37.78\,\mathrm{mm}$, width $b = 38.46\,\mathrm{mm}$ and height $h = 7.40\,\mathrm{mm}$ (cf. Fig. A.1). For the same reason, the surface of the cavity is not smooth but rather contains µm-sized grooves (not visible).

Inserting the dimensions of the cavity into Eq. (2.1) returns resonance frequencies of the eigenmodes of $f_{101} = 5.52\,\mathrm{GHz}$ and $f_{102} = 8.75\,\mathrm{GHz}$ when assuming the cavity as perfectly rectangular. A more accurate calculation is achieved by reducing the value of the width b of the cavity, such that the volume of the adjusted, rectangular cavity equals the volume of the real, curved cavity. The curvatures have the form of a semicircle, clearly visible in Fig. 3.1b. Thus, the adjusted width b' becomes

$$b' = \frac{1}{h}\left[h \cdot (b-h) + \pi\left(\frac{h}{2}\right)^2\right] = (b-h) + \frac{\pi h}{4}\,. \tag{3.1}$$

This results in theoretical resonance frequencies of $f'_{101} = 5.64\,\mathrm{GHz}$ and $f'_{102} = 8.82\,\mathrm{GHz}$.

The resonance frequencies of the TE_{103} and TE_{301} modes are located at $f'_{103} = 12.4\,\mathrm{GHz}$ and $f'_{301} = 12.8\,\mathrm{GHz}$, almost $7\,\mathrm{GHz}$ detuned from f'_{101}. This indicates that a qubit in the center position is expected to experience very little influence from modes higher than the TE_{101}, allowing for the usage of the single-mode-cavity

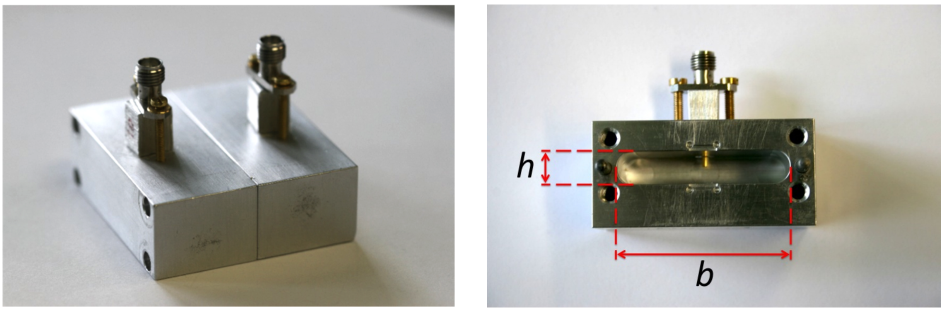

(a) (b)

Figure 3.1: (a) Closed and (b) open cavity casing with antennas, screws and spacers. The two cavity halves are held together by four bolts (missing in picture, only holes visible).

approximation when describing the circuit QED system (further elaboration in [9]). The same can be confirmed for the qubits in the TE_{102} positions.

A small trench ($6\,\mathrm{mm} \times 10\,\mathrm{mm} \times 0.5\,\mathrm{mm}$) is fabricated into the center of cavity in order to make room for a qubit wafer (visible in Fig. 3.1b and Fig. 3.2). However, the trench is of such a small size that its influence on resonance frequency and Q factor is negligible.

3.1.1 Cavity casing material

Two geometrically identical cavities are manufactured — one made of aluminum alloy (Al CuMgPb, EN AW-2007, aluminum content 88 %–93 % [22]) and the other one made of pure ($> 99.99\,\%$) aluminum.

The key feature of using aluminum or aluminum alloy is its superconducting property, where its electrical resistivity ρ becomes zero. This in turn prevents energy dissipation into the walls and consequently promotes very large Q factors. Additionally, the superconducting cavity casing shields the circuit QED system from any stray magnetic fields [23], eliminating the need for magnetic shielding equipment. Aluminum has a critical temperature of $T_\mathrm{c} = 1.98\,\mathrm{K}$ [24].

In Eq. (2.9), the dependency

$$Q_\mathrm{i} \propto \frac{1}{R_\mathrm{S}} \tag{3.2}$$

is given. In the normal-conducting state, the surface resistivity R_S is related to the resistivity ρ via $R_\mathrm{S} \propto \sqrt{\rho}$ [16], therefore

$$Q_\mathrm{i} \propto \frac{1}{\sqrt{\rho}}\,. \tag{3.3}$$

Aluminum has a resistivity of $\rho^\mathrm{Al} = 2.65 \cdot 10^{-8}\,\Omega\,\mathrm{m}$ [25] at room temperature, the aluminum alloy $\rho^{\text{alloy}} = (5.0 \pm 0.5) \cdot 10^{-8}\,\Omega\,\text{m}$ [22]. This points to a relatively high residual resistivity ρ_0 (at a temperature just above T_c) of the alloy, among the order of $\rho_0^{\text{alloy}} \approx 10^{-8}\,\Omega\,\text{m}$, compared to that of aluminum $\rho_0^{\text{Al}} = 1.0 \cdot 10^{-12}\,\Omega\,\text{m}$ [23, 25]. Due to its large impurity, we can only estimate the resistivity behavior of the alloy for lower temperatures, which likely differs significantly from the low temperature behavior of the resistivity of pure aluminum.

For the superconducting state, predictions about the surface resistivity are problematic because they highly depend on multiple factors such as the magnetic field and its frequency.

The key question is how much of an impact the purity of the aluminum cavity has on the Q factor compared to the aluminum alloy cavity — in the normal-conducting as well as the superconducting state.

3.1.2 Surface roughness

Besides the dependence of the surface resistivity on the resistivity of the material, it is also largely affected by the surface roughness of the cavity casing: smoother walls enable lower surface resistivity. Thus, because of the inverse proportionality between the Q factor and the surface resistivity, smoother walls facilitate superior Q factors.

In order to achieve a smooth surface, the aluminum alloy cavity casing is electropolished. Electropolishing is an electrochemical surface finishing method. The back of the casing half is connected to an anode while a cathode is inserted into the cavity. The casing is then submerged into a commercial electrolyte, and a current of 2.5 A at voltage 8 V is applied for 5 minutes, removing metal from the surface of the cavity and thus creating smooth cavity walls [26].

The polishing is performed at Poligrat GmbH. The pure aluminum cavity is to be electropolished at a future point in time. The goal of this endeavor is to evaluate the effect of the surface treatment on the quality factor of the resonator. Similar efforts are portrayed in [13] and [14].

3.1.3 Silicon and sapphire wafer

Two types of substrates are generally used for qubit samples: silicon and sapphire. The wafer with the qubit sample is to be placed into the trench in the center of the cavity (Fig. 3.2). We investigate the influence of substrates on the transmission parameters of the cavity. While silicon is a weak conductor at room temperature, it becomes an insulator at lower temperatures. At the same time sapphire is an insulator even at room temperature, where it has a relative permittivity of $\epsilon_\text{r} = 8.90$ (depending on its orientation) [27].

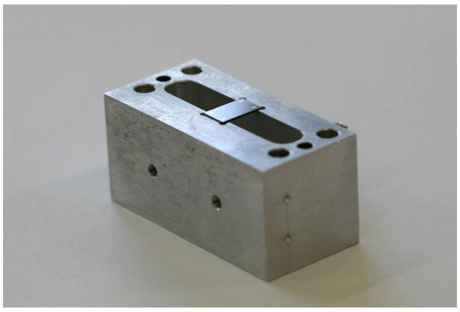

Figure 3.2: Open cavity with wafer in the center.

3.1.4 Antennas and pin depth

The cavity is coupled to the outside world via two antennas, inserted from the cavity ceiling, which are composed of standard SMA panel jacks (Rosenberger 32K722-500S5) shown in Fig. 3.3a (left). The distance between the two antennas in the cavity is 30.1 mm. They are each held in place by a pair of screws as well as a cannulated metal spacer of customizable height (Fig. 3.1b and Fig. 3.3b). This enables the modification of the pin depth p in mm, that is how far the end of the antenna reaches into the cavity. Positive p represent the antenna reaching inside the cavity, negative p describe the antenna retracted into the cavity casing, outside the cavity itself. Accordingly, p equals zero if the antenna end is flush with the cavity ceiling.

The pin depth does not noticeably affect the internal quality Q_i of the cavity itself (cf. Sec. 2.3), as the cavity properties such as volume and casing material stay the same. Instead, it heavily affects the external quality Q_c and thus the coupling strength, that is how well the microwave signal couples into the cavity [13].

The simulation in Fig. 3.4 shows Q_c to diverge for decreasing p (antenna retracting outside the cavity). This allows Q_L to converge towards Q_i, as expressed in Eq. (2.11). However, the further the antenna is retracted from the cavity, the weaker the signal that reaches the cavity. So the optimal tradeoff is found roughly at the pin depth where Q_L just about approaches Q_i, in the simulation at approximately $p = -2$ mm.

PTFE free pins

One method for optimizing the Q factor is the removal of the Polytetrafluorethylene (PTFE, relative permittivity $\epsilon_\mathrm{r} = 2.1$ [24]) from the panel jacks used as antennas, as shown in Fig. 3.3a, with the aim of minimizing dielectric losses. Subsequently, the diameter of the drilled holes that accommodate the panel jacks in the cavity and spacers needs to be adjusted in order to match impedance. The new diameter can be easily calculated (e.g., via the software AWR TX-Line).

(a) (b)

Figure 3.3: (a) SMA panel jack used as antenna (left) and panel jack with PTFE removed (right). (b) Spacers for adjustment of pin depth.

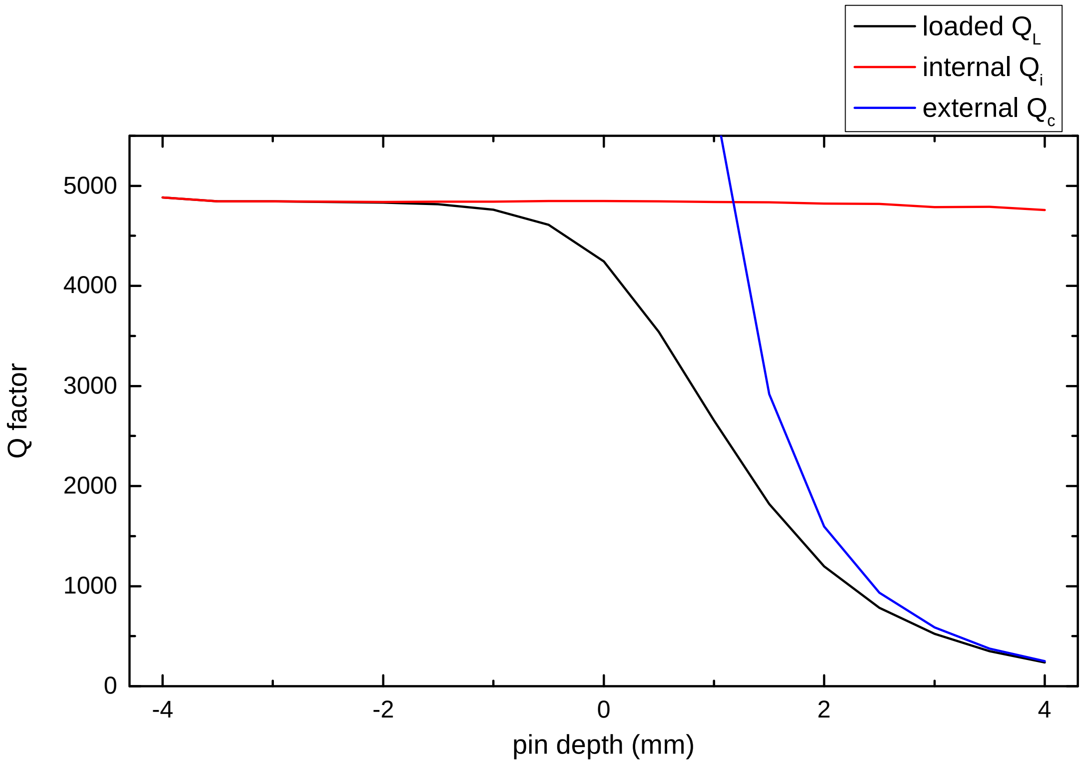

Figure 3.4: CST Microwave Studio simulation of pure aluminum cavity at room temperature. Loaded Q_L, internal Q_i and external Q_c quality factors with respect to pin depth p. Q_c diverges for decreasing pin depth, causing Q_L to approach Q_i. Q_i stays nearly constant within the investigated range.

3.2 Frequency tuning

As outlined in Sec. 2.1.2, a way of adjusting the resonance frequency of the cavity is needed in order to be able to perform certain qubit measurements. In the following, we take advantage of the dependency of the cavity resonance frequency on its dimensions and on its dielectric properties for the sake of achieving tunability.

3.2.1 Cavity gap

When closed, the two halves of the cavity casing are in full contact with each other. However, we can also keep a gap of width $\tilde{a}$ between the halves such that the length of the cavity increases to $a + \tilde{a}$ and the volume to $(a + \tilde{a}) \times b' \times h$ (cf. Sec. 3.1). As expressed in Eq. (2.1), we expect the increased length and volume of the cavity to lower its resonance frequencies.

The casing then, of course, does not fully enclose the cavity anymore: Radiation is able to enter and escape the cavity through the gap. While this is highly detrimental to actual qubit measurements, having a gap allows for quick modification of the length and thus the resonance frequencies of the cavity without having to manufacture new cavity casings. Another aspect to keep in mind is that the relative position of the antennas in the cavity also slightly changes: The larger the gap, the closer are the antennas with respect to the front and back wall of the cavity.

3.2.2 Dielectric sheet

We reuse the sapphire wafer from Sec. 3.1.3 as a dielectric sheet to insert into the cavity. We discern between two positions: center (Fig. 3.5a) and side (Fig. 3.5b). We then measure the resonance peak for both positions while varying the length s by which the sheet extends into the cavity.

In contrast to Sec. 3.1.3 we now specifically focus on the shift of the resonance peak in dependence of the sheet position and the resulting applicability for frequency tuning. Note that due to the simple method used for securing the sapphire sheet between the casing halves, a gap $\tilde{a}$ equal to the thickness of the sapphire sheet $d_S = 0.5\,\mathrm{mm}$ has to remain in the cavity.

3.3 Measurement setup

In the following, the technical details concerning the measurement setup are provided.

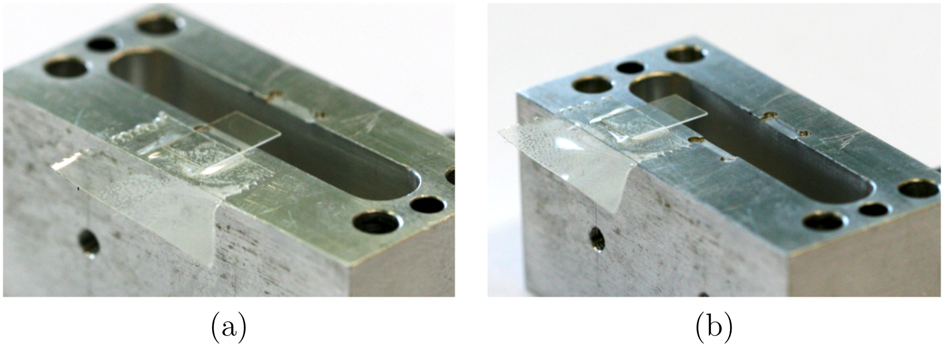

Figure 3.5: Open cavity with dielectric sapphire sheet for frequency tuning placed in (a) center and (b) side position.

3.3.1 Microwave setup

For the generation of microwaves and measurement of S-parameters, vector network analyzers (VNA) by Rohde & Schwarz (ZVA24, ZVB8) as well as Agilent Technologies (HP8772D) are used. These connect to the two antennas of the cavity through a pair of SMA cables. The SMA standard supports frequencies from DC up to 18 GHz, sufficient for this application. Key to achieving proper results is the prior through-calibration of the VNA.

For the measurements, IF Bandwidths of 100 Hz and averaging factors of either 8 or 16 are used. Typically, a frequency span of five to twenty times the FWHM of the targeted peak is measured. Also, mostly only the TE_{101} eigenmode is measured, as most conclusions can be transferred to the TE_{102} mode.

Input power

The power P_1 of the microwave signal coupled into the cavity can be set directly at the VNA. This allows us to change the input power even while the cavity is cooled down, although one has to keep in mind that the heat dissipated at higher input powers may hinder the cooling process.

The power is given in decibel-milliwatts (dBm), which converts to milliwatts (mW) via [16]

$$P_{(\mathrm{mw})} = 1\,\mathrm{mW} \cdot 10^{\left(P_{(\mathrm{dBm})}/10\right)}. \tag{3.4}$$

Generally, lower power measurements require longer measurement times to acquire accurate results, as higher averaging factors and lower IF bandwidths are needed. This especially holds true when one wants to measure at ultra-low, single photon powers.

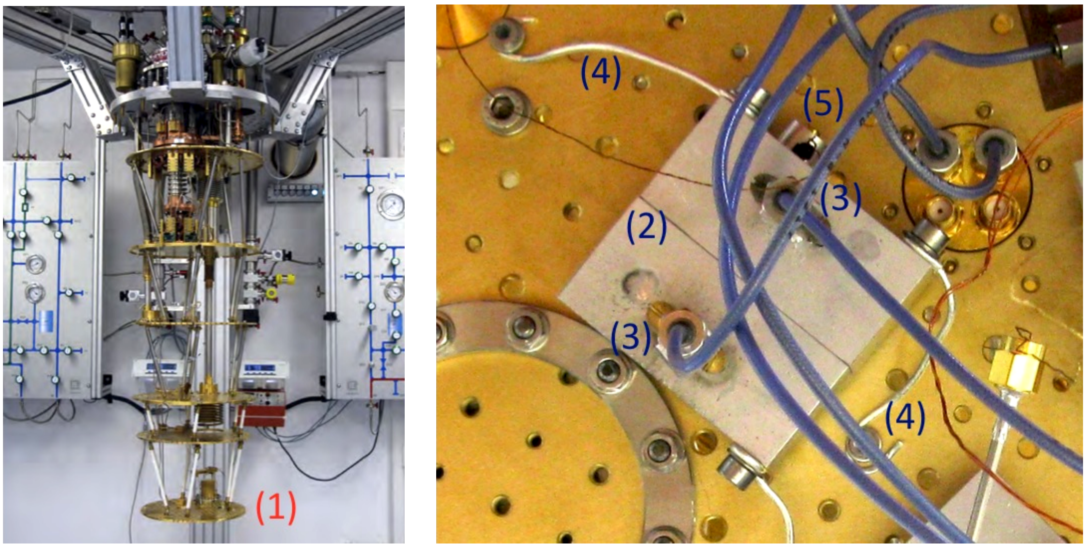

(a) (b)

Figure 3.6: Millikelvin cooldown setup: (a) ^{3}He/^{4}He dilution refrigerator with sample stage (1) at the bottom. Picture with friendly permission from [29]. (b) Cavity (2) mounted to the sample stage. Also visible are the signal ports with SMA cables connected (3), the silverwires for thermal coupling (4) and the attached temperature sensor (5).

3.3.2 Cooling methods

For the measurements at 4 K, a helium bath cryostat is used (further characterized in [28]). The core mechanism consists of immersing the cavity into a bath of liquid helium. Since the cavity casing is surrounded directly by liquid helium, it is possible that liquid helium leaks into the cavity and changes the dielectric properties of the mode volume. Liquid helium has a relative permittivity of $\epsilon_{\mathrm{r}} = 1.05$ at 4 K [24].

The measurements at millikelvin temperatures are performed in a cryogen-free ^{3}He/^{4}He dilution refrigerator, shown in Fig. 3.6a, at temperatures of approximately 60mK. Details on the cryostat can be found in [29]. In this cryostat, the cavity is located in vacuum, thermally coupled to the lowest temperature stage via silver wires (shown in Fig. 3.6b). The total attenuation of the cables in the cryostat is 57 dB. This has to be compensated by accordingly adjusted input powers. In order to reduce noise, band-pass filters with a pass band of 5.60 GHz – 7.00 GHz are placed at both ports at the cryostat and an isolator is placed at the output port.

Cooling the cavity to millikelvin temperatures is time consuming, taking up to a week for the cooling and reheating procedure. Inside the cryostat, a variation of setup parameters is mostly impossible due to the absence of physical access to the cavity — e.g., to change pin depth or amount of dielectric material inside the cavity. Thus, most of the measurements are performed at room temperature with air inside the cavity. Our line of reasoning is that the parameters which lead to best results at room temperature will be close to those that lead to best results at low temperatures. In this way, we perform measurements more efficiently, the results of which may then be verified in a vacuum at lower temperatures.

Chapter 4

Results and discussion

The results of the experiments outlined in Ch. 3 are discussed below. Note that the setup is heavily modified between experiments, particularly the pin depth p has been adjusted multiple times. Therefore, only within a single setup the measurement conditions are guaranteed to be identical, and the data is to be viewed as such. However, the conclusions of each section of course hold true for 3D cavities in general.

Unless otherwise specified, the input power is set to $-10\,\mathrm{dBm}$ and the measurement done at room temperature on the aluminum alloy cavity with air inside.

4.1 Transmission measurement and fit function

A general overview of the transmission magnitude $|S_{21}|$ is given by the frequency sweep in Fig. 4.1. The graph prominently displays the resonance peaks of the TE_{101} and TE_{102} eigenmodes. The resonance frequencies are located at $f_{101} = 5.68\,\mathrm{GHz}$ and $f_{102} = 8.88\,\mathrm{GHz}$, in close agreement with the calculated frequencies of $f'_{101} = 5.64\,\mathrm{GHz}$ and $f'_{102} = 8.82\,\mathrm{GHz}$ from Sec. 3.1. The cause for the deviation of less than $1\,\%$ can be attributed to systematic errors due to manufacturing imprecisions as well as due to the approximation made in Eq. (3.1). The presence of air in its gas phase inside the cavity has very little effect on the resonance frequency because its relative permittivity $\epsilon_\mathrm{r} = 1.00059$ [30] is very close to vacuum permittivity.

In Fig. 4.2, a fit of the squared transmission magnitude $|S_{21}|^2$ to the Lorentzian function according to Eq. (2.5) is shown. The loaded quality factor is calculated via Eq. (2.7), with the resonance frequency f_0 and FWHM Δf taken from the fit function. The Lorentzian fit function represents the data highly accurately with an adjusted coefficient of determination of, in this case, $R^2 = 0.99967$. At lower input powers, the high correlation is constrained by the comparably higher noise. In the given figure, the quality factor comes to $Q_\mathrm{L} = 3765$.

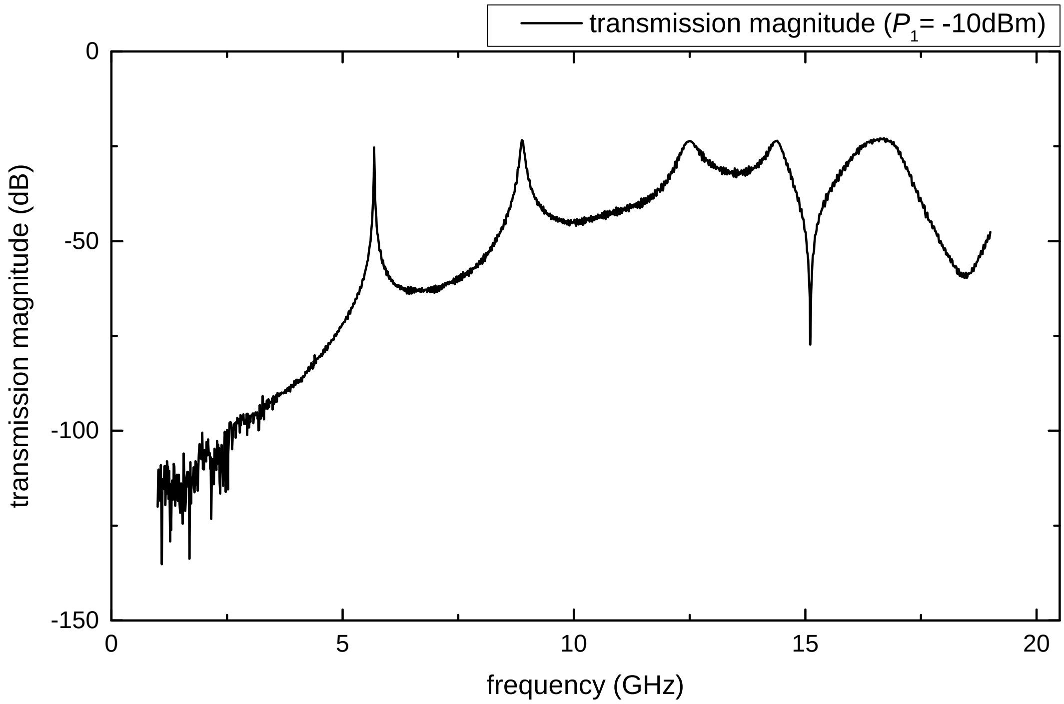

Figure 4.1: Transmission magnitude $|S_{21}|$ with respect to frequency f at input power $P_1 = -10\,\mathrm{dBm}$. The first two maxima at 5.68 GHz and 8.88 GHz represent the resonance peaks of the TE_{101} and TE_{102} eigenmodes.

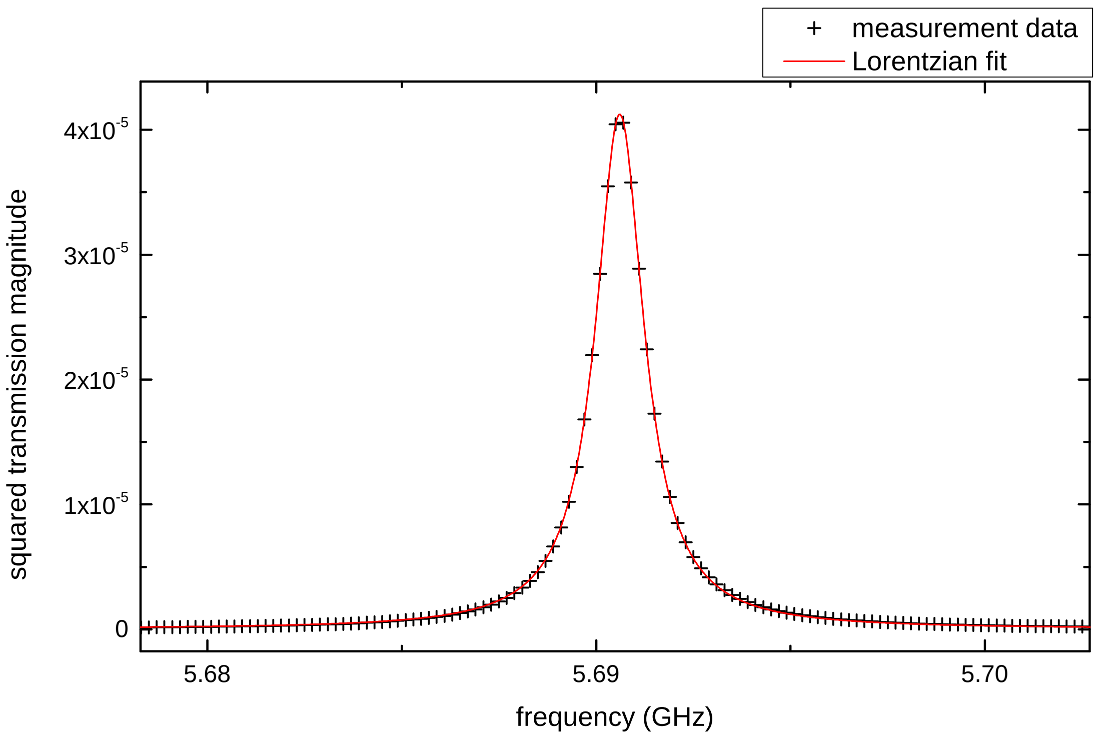

Figure 4.2: Measurement data of TE_{101} resonance peak of the squared transmission magnitude $|S_{21}|^2$ $(= \frac{P_2}{P_1})$ with Lorentzian fit function. The fit parameters provide the resonance frequency $f_{101} = 5.6906\,\mathrm{GHz}$ and FWHM $\Delta f = 1.5113\,\mathrm{MHz}$. The corresponding loaded quality factor is $Q_\mathrm{L} = 3765$.

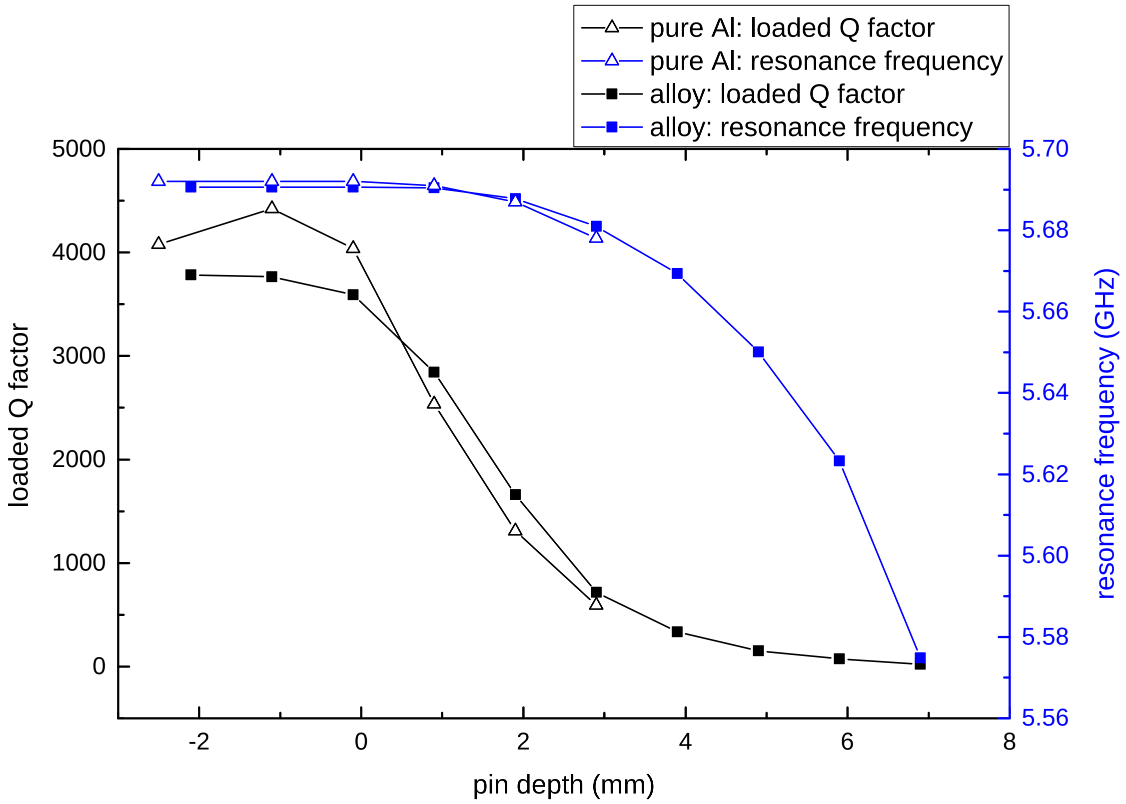

Figure 4.3: Loaded quality factor Q_L and resonance frequency f_{101} of the pure aluminum as well as the aluminum alloy cavity with respect to pin depth p.

4.2 Cavity properties

We now evaluate the characteristics of the cavity as described in Sec. 3.1.

4.2.1 Cavity casing material

First, we examine the differences between the two casing materials. Figure 4.3 shows a pin depth sweep for the alloy and the pure cavity at room temperature. The behavior of the loaded quality factors Q_L resembles the simulation displayed in Fig. 3.4. The alloy cavity reaches quality factors up to $Q_\mathrm{L} = 3770$, whereas the pure aluminum cavity reaches up to $Q_\mathrm{L} = 4423$, an increase by 17 % over the alloy cavity. According to the resistivity of the materials as discussed in Sec. 3.1.1, a difference of at least 30 % would be expected between the two materials. The smaller difference may be explained by the manufacturing process, which creates a different surface roughness for the two different materials.

The resonance frequencies f_{101} of the two cavities are virtually identical, deviating by less than 0.1 % from each other. Although the respective resonance frequencies decrease for higher pin depths, this characteristic is unsuitable for frequency tuning,

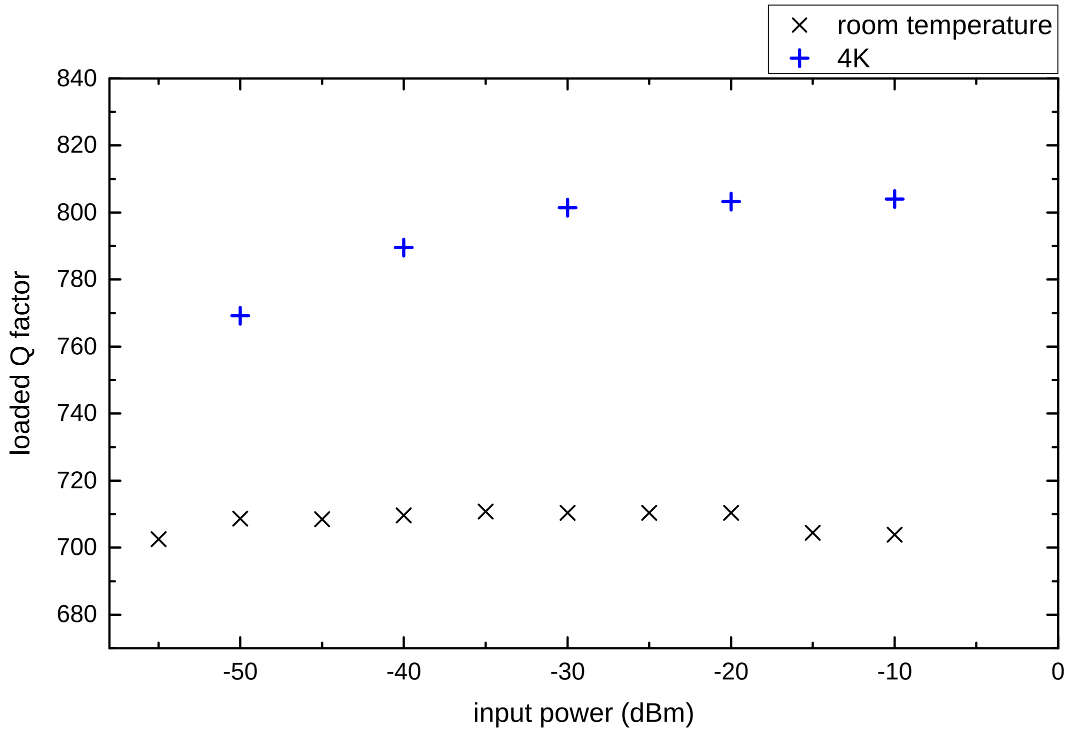

Figure 4.4: Loaded quality factor Q_L as a function of input power P_1 at room temperature as well as temperature $T = 4\,\mathrm{K}$.

since the loaded quality factor Q_L suffers substantially from higher pin depths, quickly approaching zero.

4.2.2 Surface roughness

The electropolishing of the aluminum alloy cavity prompts an increase in quality factor by approximately $4\,\%$ from $Q_\mathrm{L} = 3770$ to 3919. The comparably little rise in quality can be explained by the nature of the AlCuMgPb alloy: During the electropolishing process, the aluminum and copper atoms are etched off the surface far more freely than e.g., the lead atoms. This causes an actual increase in surface roughness instead of the desired decrease — the average roughness of the alloy cavity has increased from $R_a = 0.295\,\mu\mathrm{m}$ to $0.649\,\mu\mathrm{m}$, measured at the center of the cavity bottom. So the macroscopic polishing is accompanied by the creation of a microscopically rugged surface. A similar lack of improvement when treating alloys can be found in [14].

4.2.3 Input power

We now sweep the power P_1 of the input signal. The resulting Q factor of the aluminum alloy cavity at room temperature as well as $4\,\mathrm{K}$ is plotted in Fig. 4.4.

We observe that the quality factor remains fairly constant, fluctuating by less than 1 % at room temperature and less than 5 % at 4 K for powers between −10 dBm and −55 dBm. Lower powers do not yield enough signal to obtain reliable results. Notably, no superconducting properties can be observed from the aluminum alloy cavity at 4 K, as a quality factor multiple orders of magnitude higher would be expected. Hence, the critical temperature T_c of the alloy lies below 4 K.

The measurements show that, at least for an input power higher than −55 dBm, the quality factor remains stable, as desired. The data does not offer a result for lower powers. However, in [14] the same power independence is found even at single photon powers. This poses an advantage over planar resonators, where frequency and lifetime depend on power.

4.2.4 Silicon and sapphire wafer

Figure 4.5 shows the transmission magnitude $|S_{21}|$ for the cavity without wafer and with a silicon wafer inside. The conducting silicon completely suppresses the TE_{101} mode, which is supposed to have its maximum of the electric field exactly where the wafer is placed: at the very center of the cavity. Nevertheless, a measurement with the silicon wafer inside the cavity taken at a temperature of $T = 4\,\mathrm{K}$ results in a quality factor of $Q_\mathrm{L} = 947$, confirming the TE_{101} mode to reappear as silicon becomes insulating at lower temperatures.

Also visible in Fig. 4.5 is the fact that the TE_{102} mode at 8.88 GHz is unaffected by the conducting wafer in the center, as its electric field is zero at the wafer position. The resonance frequency f_{102} of the TE_{102} mode increases slightly due to the wafer reducing the cavity volume as well as due to the inserted dielectric material.

The measurements with a dielectric sapphire wafer at room temperature yield a quality factor of $Q_\mathrm{L} = 728$, compared to $Q_\mathrm{L} = 716$ without wafer. These results verify that the quality factor remains nearly unchanged by the insertion of a dielectric wafer.

4.2.5 PTFE free pins

The removal of the PTFE from the panel jacks used as antennas, as shown in Fig. 3.3a, leaves the quality factor virtually unchanged. The increase of less than 0.3 % (from $Q_\mathrm{L} = 3704$ to 3714) lies well within the error of our measurement. As described in Sec. 3.1.4, one would then have to adjust the diameter of the holes that accommodate the panel jacks for impedance matching. However, due to the negligible effect observed in the non-matched measurement, this approach is not pursued any further — only unmodified antennas wrapped with PTFE are used for the other measurements.

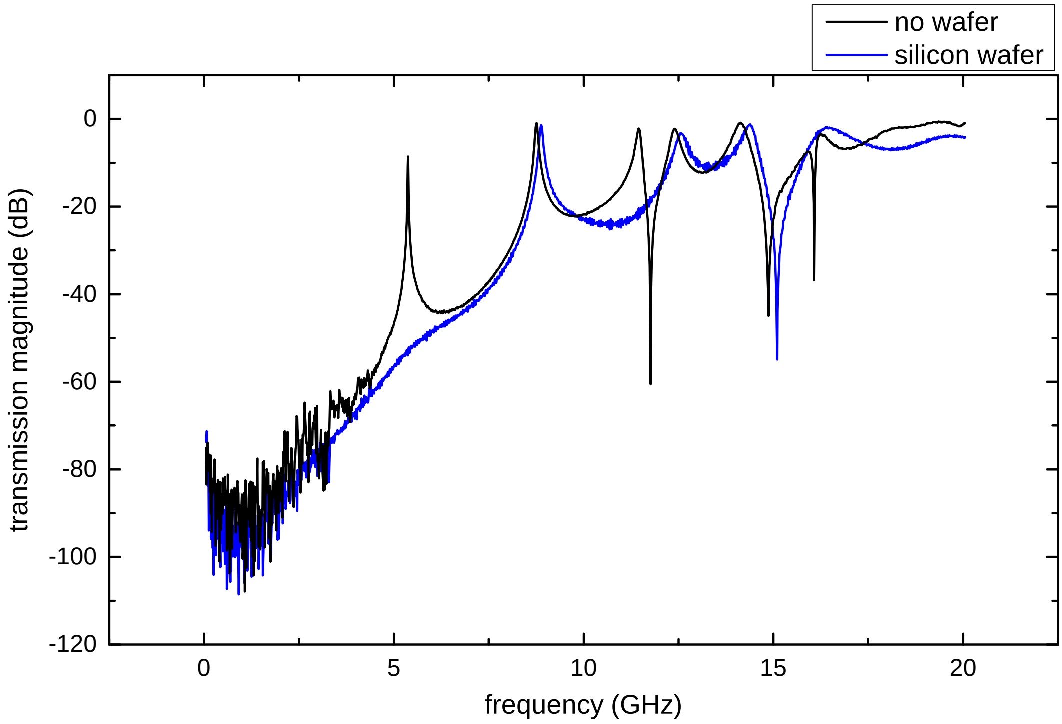

Figure 4.5: Transmission magnitude $|S_{21}|$ with respect to frequency f at room temperature without wafer and with conducting silicon wafer in the center. The TE_{101} mode at 5.68 GHz disappears, the TE_{102} mode at 8.88 GHz shifts by a frequency of 0.11 GHz.

4.3 Frequency tuning

For the two methods of frequency tuning we now focus on the frequency shifts caused by the specific setups. Here we do not aim for maximum Q factor, but rather a stable Q factor independent from the changes in the setup.

4.3.1 Cavity gap

Quality factor Q_{L} as well as measured and calculated resonance frequency f_{101} with respect to gap width are shown in Fig. 4.6. As predicted, the resonance frequency of the cavity declines for increasing gap widths $\tilde{a}$. As we can see, small changes in volume already cause noteworthy shifts in resonance frequency, covering the ranges required for frequency tuning (cf. Sec. 2.1.2). The measured frequencies fit the calculations within an error of less than 0.3 %, although the deviation increases for larger gaps.

Interestingly, the Q factor increases significantly for larger gap widths, despite letting microwave radiation escape the cavity. While this might be related to the relative change in position of the antennas — withdrawing them from the electrical field of the TE_{101} mode — this behavior is yet to be explained with definite confidence.

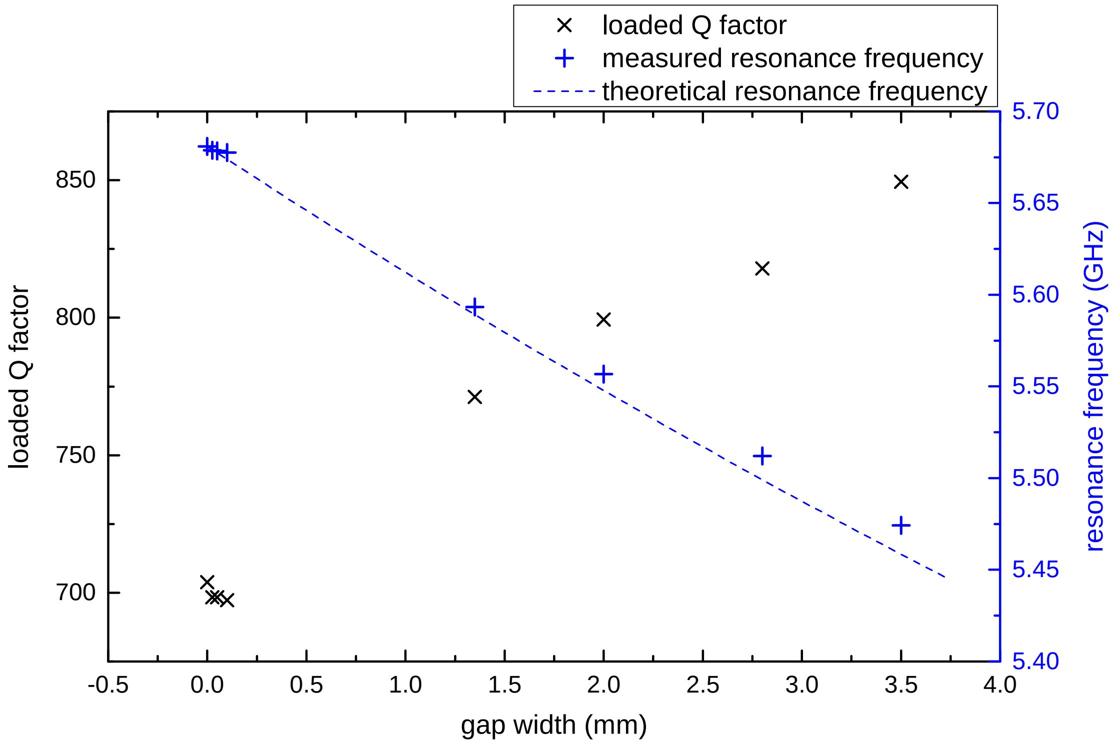

Figure 4.6: Loaded quality factor Q_L as well as measured and calculated resonance frequency f_{101} of TE_{101} with respect to gap width $\tilde{a}$. The theoretical resonance frequency is calculated according to Eq. (2.1) and adjusted by the systematical offset of 36 MHz discussed in Sec. 4.1.

The large dependence of the resonance frequency on the cavity length, as well as no sign of negative impact on the Q factor, attest high suitably of this mechanism for frequency tuning. A more elaborate method of changing the volume than the one utilized here is proposed in Ch. 5.

4.3.2 Dielectric sheet

Figure 4.7 shows the different quality factors Q_L and resonance frequencies f_{101} of the aluminum alloy cavity, caused by inserting a dielectric sheet to a length s into the cavity in center and side position (cf. Fig. 3.5).

We see that the Q factor fluctuates slightly more for the side position. Nevertheless, the total variation of the Q factor is less than 2 %. Since the electric field of the TE_{101} mode is decreasing away from the center, the resonance frequency shift is far lower for the side position: It shifts by less than 30 MHz when the sheet is almost completely inside the cavity (total height of the cavity: 7.40 mm).

At the center position we observe a very stable Q factor, deviating by less than 0.5 % across the four sheet depths measured. Also, the resonance frequency spans a

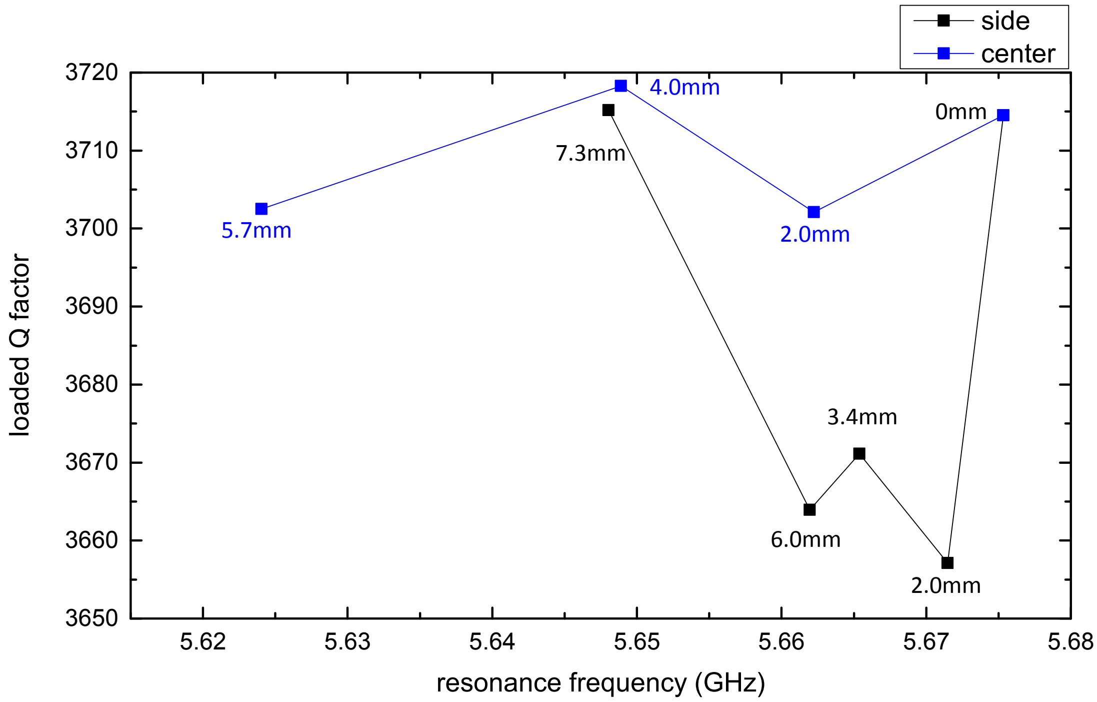

Figure 4.7: Loaded quality factor Q_L for different resonance frequencies f_{101} as well as corresponding sheet depth s (data point labels), side and center position (cf. Fig. 3.5). The cavity has a gap of $\tilde{a} = 0.5\,\mathrm{mm}$, equal to the thickness of the sapphire sheet.

range of more than 60 MHz, considerably more than in the side position. Both of these characteristics make the insertion of a dielectric sheet highly appealing for use in frequency tuning. However, note that in the center position, the sapphire sheet would be placed on top of the qubit in later experiments. Whether this affects the circuit QED configuration negatively is yet to be tested. In that case, other sheet positions close to the maximum of the TE_{101} mode may perform better.

4.4 Millikelvin cooldown

Finally, we examine the data gathered from cooling the aluminum alloy cavity in the dilution refrigerator. At the time of the cooldown, the cavity has not been electropolished. The pin depth is set at $p = -2.1\,\mathrm{mm}$. Figure 4.8 shows the quality factor and resonance frequency over a temperature range from 163 K to 27 K.

The resonance frequency rises due to thermal contraction of the cavity casing. The thermal expansion coefficient tapers off for temperatures approaching zero Kelvin [23], explaining the flattening out of the plotted resonance frequency curve for lower temperatures. The resonance frequency of the alloy with respect to temperature can be approximated by a polynomial of the fourth order (also plotted) [31]. The low-temperature thermal contraction coefficient of the alloy, deduced from its resonance

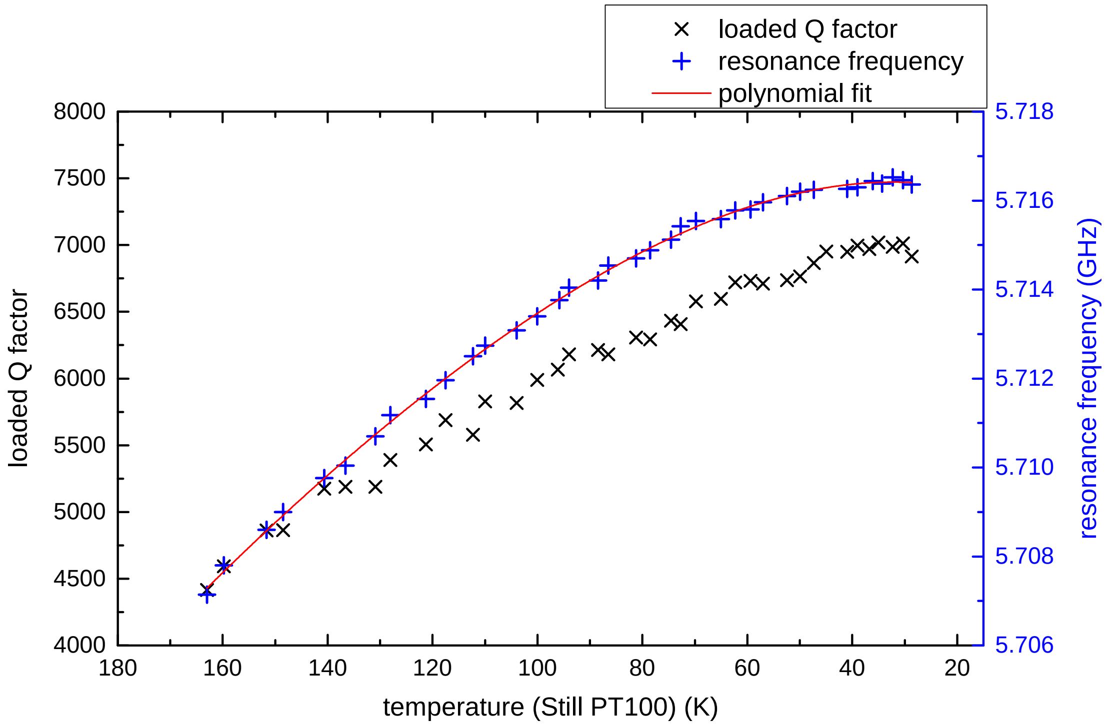

Figure 4.8: Loaded quality factor Q_L as well as resonance frequency f_{101} of the aluminum alloy cavity at temperature T as measured by the sensor "Still PT100". Fourth order polynomial fitted to measured resonance frequencies.

frequencies, conforms to literature values [31] remarkably well with a maximum deviation of less than 0.05 %.

The loaded Q factor rises steadily with decreasing temperatures, down to $\sim 27\,\mathrm{K}$, corresponding to the decreasing surface resistivity. The cavity reaches a maximum Q factor of $Q_\mathrm{L} = 7013$ above $27\,\mathrm{K}$, an increase by a factor of 1.9 over the Q factor at room temperature. This yields an approximate value for the residual resistivity of $\rho_0(27\,\mathrm{K}) \approx (1.4 \pm 0.2) \cdot 10^{-8}\,\Omega\,\mathrm{m}$ for the alloy used for the casing. Note that the Q factor above T_c is limited by the residual resistivity ρ_0 of the alloy. For the pure aluminum cavity, an increase of the Q factor by a factor well within the order of 10 is expected from room temperature to $20\,\mathrm{K}$, highly depending though on the actual purity of the used aluminum and the resulting resistivity (cf. Sec. 3.1.1) [16, 23, 25].

In Fig. 4.9 the TE_{101} resonance peak at $T = 60\,\mathrm{mK}$ and $P_\mathrm{l} = -65\,\mathrm{dBm}$ is shown. A superb quality factor of $Q_\mathrm{L} = 341\,000$ is achieved, with a FWHM of $\Delta f_{101} = 16.8\,\mathrm{kHz}$. This corresponds to a theoretical photon lifetime of $\tau = 9.49\,\mu\mathrm{s}$ inside the cavity. However, at this point it remains unclear whether the cavity coupling in fact stays unchanged for decreasing and especially for millikelvin temperatures. Thus, Q_i could possibly be even higher than the measure Q_L, implying even longer photon lifetimes.

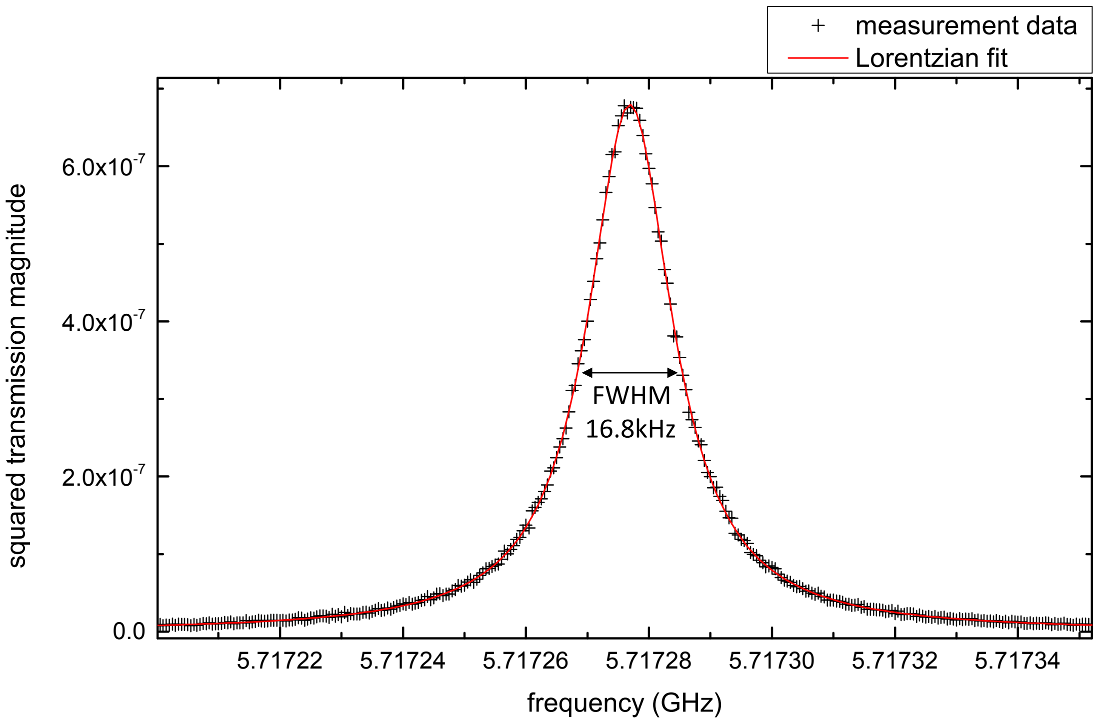

Figure 4.9: Superconducting aluminum alloy cavity at temperature of $T = 60\,\mathrm{mK}$ and input power at cavity of $P_1 = -65\,\mathrm{dBm}$: resonance peak of $|S_{21}|^2 = \frac{P_2}{P_1}$. The resonance frequency is located at $f_{101} = 5.717\,277\,\mathrm{GHz}$. Demonstration of Lorentzian fit used to acquire a FWHM of $16.8\,\mathrm{kHz}$ and quality factor of $Q_\mathrm{L} = 341\,000$.

Chapter 5

Conclusions and outlook

Finally, we summarize the insights gained during this thesis and take a look at possible improvements for the near future.

We investigate the transmission properties of two aluminum cavities intended for circuit QED experiments. Aside from a general characterization, the high applicability of the theoretical models describing the cavity have been verified, such as the use of a Lorentzian fit function and the calculation of the resonance frequency with respect to changing volume and temperature. The quality factor has been found to be independent from input power, dielectric wafer as well as dielectric around the antennas. Dependencies of the internal Q factor on surface resistivity, surface roughness, resistivity and temperature have been confirmed.

Furthermore, a way of adjusting the coupling coefficient by changing the pin depth of the antennas has been established via simulation and experiments. Prominently, two methods of frequency tunability have been demonstrated: by changing the length of the cavity as well as by adjusting the amount of dielectric inside the cavity. Also, an outstanding quality factor of $Q_\mathrm{L} = 3.4 \cdot 10^{10}$ has been achieved with the unoptimized aluminum alloy cavity.

The theoretical considerations as well as the experiments performed during this project lay the foundations for future improvements:

First and foremost, eyes are now on the pure aluminum cavity, for which quality factors far exceeding those of the alloy cavity are expected. When electropolishing the pure aluminum cavity, the material is removed from the walls consistently, creating a high-caliber smooth surface. In [14], similarly treated aluminum cavities yielded quality factors of up to $Q_\mathrm{L}^\mathrm{Al} = 6.1 \cdot 10^7$. In the same paper, quality factors of up to $Q_\mathrm{i} \approx 10^9$, corresponding to photon lifetimes of $\tau > 0.1\,\mathrm{s}$, are assumed to be possible.

A further candidate for the cavity material is copper, which provides better thermal coupling than aluminum. Nevertheless, it does not become superconducting and therefore does not produce comparably large Q factors (recently up to $Q_\mathrm{L}^\mathrm{Cu} = 9.2 \cdot 10^4$ [13]). However, the influence of the lower Q factor can be lessened through minimizing the Purcell effect by detuning the qubit from the cavity mode frequency [13].

Another prospect is the seemingly easy possibility of frequency tuning the cavity.

While the methods used in this thesis are not practical for use in qubit measurements, they certainly prove the viability of similar approaches.

The next step for the gap method employed in Sec. 3.2.1 and Sec. 4.3.1 would be to exchange one of the walls of the cavity with a thin plate of the same casing material. Then, a piezomotor can apply an adjustable, constant force onto the plate from outside the cavity, elastically bending the plate inside and thus changing the cavity volume. This approach would provide the possibility for in-situ frequency tuning even at millikelvin temperatures.

Similarly, the tuning via dielectric outlined in Sec. 3.2.2 and Sec. 4.3.2 may be expanded upon by letting a piezomotor push the sheet in and out, enabling in-situ tuning via this method as well.

All in all, 3D cavities show tremendous potential and certainly pose a huge step forward in the field of circuit quantum electrodynamics, pushing the boundaries imposed by coherence times. Combined with advancements that repress decay channels other than the cavity quality factor, qubit lifetimes of up to 0.1 ms are now achievable [9] — considerably higher than previously possible [7, 12].

Appendix

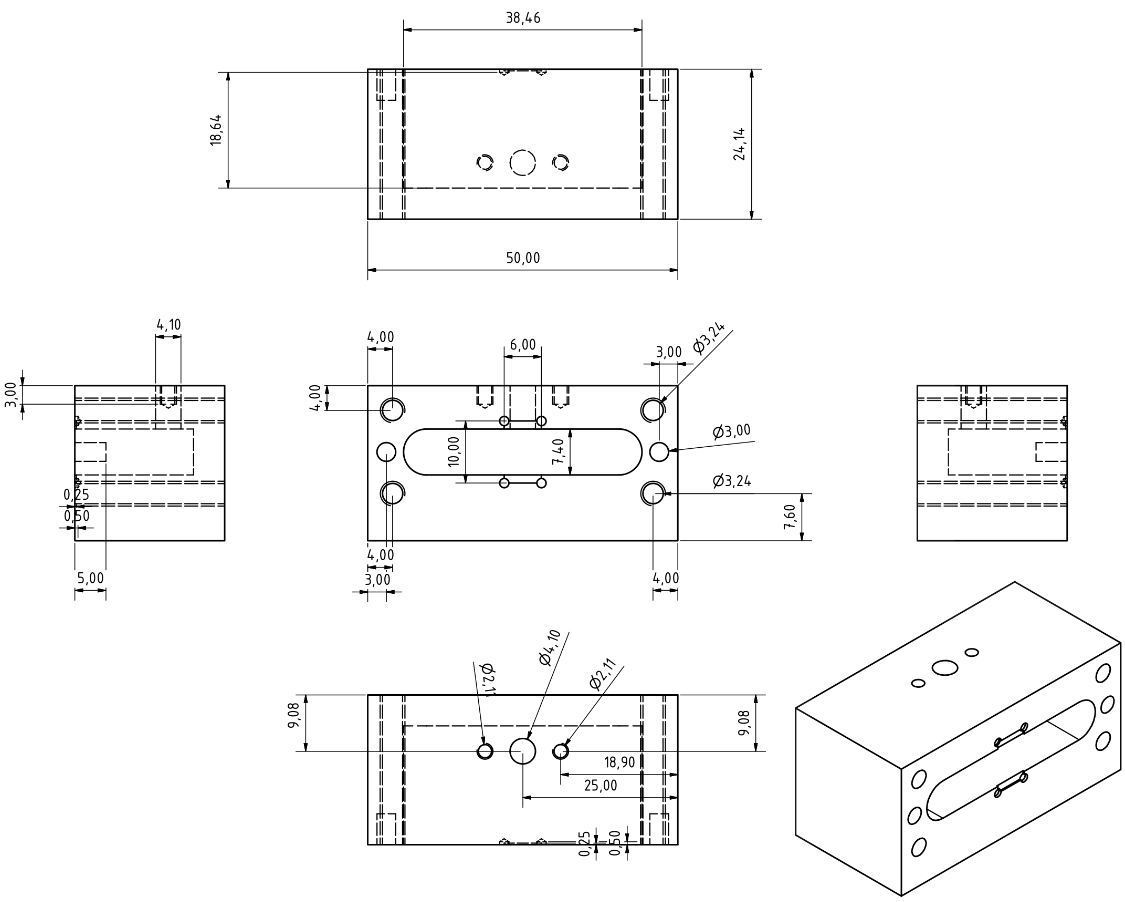

Figure A.1: Technical drawing of a cavity casing half. Dimensions in mm. Cavity has length $a = 37.78\,\text{mm}$, width $b = 38.46\,\text{mm}$ and height $h = 7.40\,\text{mm}$. Due to its two curved sides, the cavity is not perfectly rectangular. The trench ($6\,\text{mm} \times 10\,\text{mm} \times 0.5\,\text{mm}$) in the center of the cavity accommodates the wafer.

Bibliography

[1] Micheal A. Nielsen and Isaac L. Chuang, *Quantum Computation and Quantum Information* (Cambridge University Press, Cambridge, 2000), 7th ed.

[2] J. Clarke and F. K. Wilhelm, "Superconducting quantum bits", Nature **453**, 1031 (2008).

[3] A. Blais, R.-S. Huang, A. Wallraff, S. M. Girvin, and R. J. Schoelkopf, "Cavity quantum electrodynamics for superconducting electrical circuits: An architecture for quantum computation", Phys. Rev. A **69**, 062320 (2004).

[4] A. Wallraff, D. I. Schuster, A. Blais, L. Frunzio, R. S. Huang, J. Majer, S. Kumar, S. M. Girvin, and R. J. Schoelkopf, "Strong coupling of a single photon to a superconducting qubit using circuit quantum electrodynamics", Nature **431**, 162 (2004).

[5] R. J. Schoelkopf and S. M. Girvin, "Wiring up quantum systems", Nature **451**, 664 (2008).

[6] T. Niemczyk, F. Deppe, H. Huebl, E. P. Menzel, F. Hocke, M. J. Schwarz, J. J. Garcia-Ripoll, D. Zueco, T. Hummer, E. Solano, A. Marx, and R. Gross, "Circuit quantum electrodynamics in the ultrastrong-coupling regime", Nat. Phys. **6**, 772 (2010).

[7] R. Barends, J. Kelly, A. Megrant, D. Sank, E. Jeffrey, Y. Chen, Y. Yin, B. Chiaro, J. Mutus, C. Neill, P. O'Malley, P. Roushan, J. Wenner, T. C. White, A. N. Cleland, and J. M. Martinis, "Coherent Josephson Qubit Suitable for Scalable Quantum Integrated Circuits", Phys. Rev. Lett. **111**, 080502 (2013).

[8] H. Paik, D. I. Schuster, L. S. Bishop, G. Kirchmair, G. Catelani, A. P. Sears, B. R. Johnson, M. J. Reagor, L. Frunzio, L. I. Glazman, S. M. Girvin, M. H. Devoret, and R. J. Schoelkopf, "Observation of High Coherence in Josephson Junction Qubits Measured in a Three-Dimensional Circuit QED Architecture", Phys. Rev. Lett. **107**, 240501 (2011).

[9] C. Rigetti, J. M. Gambetta, S. Poletto, B. L. T. Plourde, J. M. Chow, A. D. Córcoles, J. A. Smolin, S. T. Merkel, J. R. Rozen, G. A. Keefe, and et al.,

"Superconducting qubit in a waveguide cavity with a coherence time approaching 0.1 ms", Phys. Rev. B **86** (2012).

[10] G. Kirchmair, B. Vlastakis, Z. Leghtas, S. E. Nigg, H. Paik, E. Ginossar, M. Mirrahimi, L. Frunzio, S. M. Girvin, and R. J. Schoelkopf, "Observation of quantum state collapse and revival due to the single-photon Kerr effect", Nature **495** (2013).

[11] A. P. Sears, A. Petrenko, G. Catelani, L. Sun, H. Paik, G, Kirchmair, L. Frunzio, L. I. Glazman, S. M. Girvin, and R. J. Schoelkopf, "Photon Shot Noise Dephasing in the Strong-Dispersive Limit of Circuit QED", Phys. Rev. B **86**, 180504 (2012).

[12] K. L. Geerlings, "Improving Coherence of Superconducting Qubits and Resonators", Ph.D. thesis, Yale University (2013), URL `http://qulab.eng.yale.edu/documents/theses/Kurtis_ImprovingCoherenceSuperconductingQubits.pdf`.

[13] D. F. Bogorin, M. Ware, D. T. McClure, S. Sorokanich, and B. L. T. Plourde, "Reducing surface loss in 3D microwave copper cavities for superconducting transmon qubits", ISEC **14**, 1 (2013).

[14] M. Reagor, H. Paik, G. Catelani, L. Sun, C. Axline, E. Holland, I. M. Pop, N. A. Masluk, T. Brecht, L. Frunzio, M. H. Devoret, L. Glazman, and R. J. Schoelkopf, "Reaching 10 ms single photon lifetimes for superconducting aluminum cavities", Appl. Phys. Lett. **102**, 192604 (2013).

[15] J. Home and B. Keitch, "Cavity QED and Ion Trap Physics, Lecture Notes", (2012).

[16] D. M. Pozar, *Microwave engineering* (John Wiley & Sons, Inc, New York, 1998), chap. Microwave Resonators, pp. 300–350, 2nd ed.

[17] B. Vlastakis, G. Kirchmair, Z. Leghtas, S. E. Nigg, L. Frunzio, S. M. Girvin, M. Mirrahimi, M. H. Devoret, and R. J. Schoelkopf, "Deterministically Encoding Quantum Information Using 100-Photon Schrödinger Cat States", Science **342**, 607 (2013).

[18] A. Mezzacapo, L. Lamata, S. Filipp, and E. Solano, "Many-Body Interactions with Tunable-Coupling Transmon Qubits", ArXiv e-prints:abs/1403.3652 (2014).

[19] P. J. Petersan and S. M. Anlage, "Measurement of Resonant Frequency and Quality Factor of Microwave Resonators: Comparison of Methods", J. Appl. Phys. **84**, 3392 (1998).

[20] T. Jungkunz and G. Fischerauer, “Resonance parameter estimation for low-Q microwave cavities”, SSD **9**, 1 (2012).

[21] B. Saleh and M. Teich, *Fundamentals of photonics* (John Wiley & Sons, Inc, New York, 1991), chap. Resonator Optics, pp. 310–341, 1st ed.

[22] W. Hesse and D. V, *Aluminium-Werkstoff-Datenblätter: Deutsch / Englisch* (Beuth Verlag GmbH, Berlin, 2011), pp. 32–35, Beuth Wissen, 6th ed.

[23] R. Gross and A. Marx, *Festkörperphysik* (Oldenburg Wissenschaftsverlag GmbH, Munich, 2012), 1st ed.

[24] D. R. Lide, *CRC Handbook of Chemistry and Physics, Internet Version* (CRC Press, Boca Raton, FL, 2005), 85th ed., URL http://www.hbcpnetbase.com.

[25] P. D. Desai, H. M. James, and C. Y. Ho, “Electrical Resistivity of Aluminum and Manganese”, J. Phys. Chem. Ref. Data **13**, 1131 (1984).

[26] *Poligrat Electropolishing*, brochure, Poligrat GmbH (2004), URL http://www.poligrat.co.uk/media/Broschueren/en_brochures/Brochure%20%20english%20-%20Electropolishing.pdf.

[27] A. K. Harman, S. Ninomiya, and S. Adachi, “Optical constants of sapphire (alpha-Al2O3) single crystals”, J. Appl. Phys. **76**, 8032 (1994).

[28] E. C. M. Hoffmann, “Experiments on Two-Resonator Circuit Quantum Electrodynamics: A Superconducting Quantum Switch”, Ph.D. thesis, Technische Universität München (2013), URL http://www.wmi.badw.de/publications/theses/Hoffmann,Elisabeth_Doktorarbeit_2013.pdf.

[29] *Annual Report 2013*, Walther-Meißner-Institute for Low Temperature Research (2013), URL http://www.wmi.badw-muenchen.de/publications/jahresberichte/2013.pdf.

[30] L. G. Hector and H. L. Schultz, “The Dielectric Constant of Air at Radiofrequencies”, J. Appl. Phys. **7**, 133 (1936).

[31] E. D. Marquardt, J. P. Le, and R. Radebaugh, “Cryogenic Material Properties Database”, ICC **11**, 681 (2002).

Acknowledgements

First of all I would like to thank the director of the WMI, Prof. Dr. Rudolf Gross for granting me the opportunity of writing this thesis at the WMI, but also for the excellent teaching of the condensed matter physics lecture during the past two semesters, bringing much enjoyment and unique insights.

Many thanks go to my supervisor Edwar Xie for his continuous guidance, truly going out of his way to help me out with countless experiments, calculations and background questions as well as everything else related to this thesis. I highly appreciate the amounts of time and effort he spent, offering a very hands-on approach and guaranteeing everything to go as smoothly as possible.

I also want to thank Gustav Andersson for the collaboration in doing experiments and calculations, but also for doing the numerous simulations related to this thesis. Also, the many talks we had often led to new ideas and perspectives.

Further thanks go to Dr. Achim Marx — on the one hand for offering me the working student job at the WMI and spending lots of time introducing me to the practical side of the circuit QED research field and on the other hand for offering me this thesis and overseeing the dilution refrigerator experiments.

Similarly, thanks to Ling Zhong and Dr. Kirill Fedorov for the extensive assistance concerning the dilution refrigerator.

Additional thanks to Dr. Frank Deppe for proofreading this thesis, keeping a keen eye on language as well as content.

Likewise, I want to thank all the other people at the WMI and especially the qubit group for their plentiful input as well as the very enjoyable working atmosphere.

Lastly, I thank my parents for supporting me as well as giving me the possibility to study physics in Munich.